

Stability of Pinned Surface Nanobubbles Against Expansion: Insights from Theory and Simulation

Yawei Liu,^{1,*} Stefano Bernardi,^{1,†} and Asaph Widmer-Cooper^{1,2,‡}

¹*ARC Centre of Excellence in Exciton Science, School of Chemistry,
University of Sydney, Sydney, New South Wales 2006, Australia*

²*The University of Sydney Nano Institute, University of Sydney, Sydney, New South Wales 2006, Australia*

While growth and dissolution of surface nanobubbles has been widely studied in recent years, their stability under pressure changes or a temperature increase has not received the same level of scrutiny. Here, we present theoretical predictions based on classical theory for pressure and temperature thresholds (p_c and T_c) at which unstable growth occurs for the case of air nanobubbles on a solid surface in water. We show that bubbles subjected to pinning have much lower p_c and higher T_c compared to both unpinned and bulk bubbles of similar size, indicating that pinned bubbles can withstand a larger tensile stress (negative pressure) and higher temperatures. The values of p_c and T_c obtained from many-body dissipative particle dynamics (MDPD) simulations of quasi-two-dimensional (quasi-2D) surface nanobubbles are consistent with the theoretical predictions, provided that the lateral expansion during growth is taken into account. This suggests that the modified classical thermodynamic description is valid for pinned bubbles as small as several nanometers. While some discrepancies still exist between our theoretical results and previous experiments, further experimental data is needed before a comprehensive understanding of the stability of surface nanobubbles can be achieved.

I. INTRODUCTION

The stability of surface nanobubbles has been a controversial topic since the work of Parker *et al.* in 1994 [1], but it experienced renewed interest after the first AFM images were obtained in 2000 [2, 3]. Nanoscale bubbles at solid-water interfaces are predicted to be unstable due to an extremely high inner pressure. For example, according to the Epstein-Plesset theory [4], the lifetime of bubbles smaller than 1000 nm in water should be less than 0.02 s, which would also make their experimental detection extremely difficult [5, 6]. However, many experimental techniques including AFM [2, 3, 7], rapid cryofixation [8], neutron reflectometry [9], and direct optical visualization [10, 11] have confirmed that surface nanobubbles can exist for hours or even days.

In 2013, experimental, theoretical, and computational studies proved the contact line pinning effect to be crucial for the stability of surface nanobubbles [12–14]. Pinned bubbles, whose contact line is anchored by surface heterogeneities, can reach thermodynamically stable states under oversaturation, or dissolve on a much longer timescale than bulk bubbles when undersaturated. Since 2013, an impressive number of studies of surface nanobubbles have been performed to investigate the contact line pinning effect [15–23]. These studies examined surface nanobubbles under pressures and temperatures at which they were expected to dissolve due to gas diffusion, but were instead found to be stable. Two experimental papers studied the evolution of surface nanobubbles under pressure reduction (i.e., in the cavitation regime) and temperature increase. At a specific pressure or temperature threshold (p_c and T_c), the bubble undergoes expansion and suffers an unstable and uncontrolled growth. As early as 2007, Borkent *et al.*

reported that surface nanobubbles do not cavitate down to -6 Mpa [24], a much lower value than the Blake threshold below which a bulk bubble with the same radius of curvature starts to grow unbounded [25, 26]. In 2014, Zhang *et al.* unexpectedly observed that surface nanobubbles also remain stable when the temperature increases up to a value close to the boiling point of water [27]. However, despite the surprising stability that surface nanobubbles have shown against expansion induced by both pressure reduction and temperature increase (referred to as *superstability* in Ref. [24, 27]), only a few studies have been dedicated to this phenomenon so far. One reason for this may be the lack of experimental techniques capable of probing surface nanobubbles without perturbing them.

More recently, using molecular dynamics simulations, Dockar *et al.* [28] studied the mechanical stability of surface nanobubbles pinned on patterned substrates and exposed to a pressure reduction. They found a much lower p_c than that predicted by the Blake threshold. Their simulation results agreed with a corrected cavitation threshold they derived for pinned bubbles. In this work, we investigate the stability of pinned surface nanobubbles under pressure reduction as well as temperature increase by extending the classical theory to pinned bubbles and using particle dynamics simulations. We first present a theoretical analysis of p_c and T_c for both unpinned and pinned surface nanobubbles. The stability of surface nanobubbles in water is discussed in detail based on the theoretical calculations. We then present results for p_c and T_c obtained from many-body dissipative particle dynamics (MDPD) simulations of quasi-two-dimensional (quasi-2D) pinned surface nanobubbles and compare them with the corresponding theoretical predictions. Finally, we compare our results with earlier studies, including experimental work.

* yawei.liu@sydney.edu.au

† stefano.bernardi@sydney.edu.au

‡ asaph.widmer-cooper@sydney.edu.au

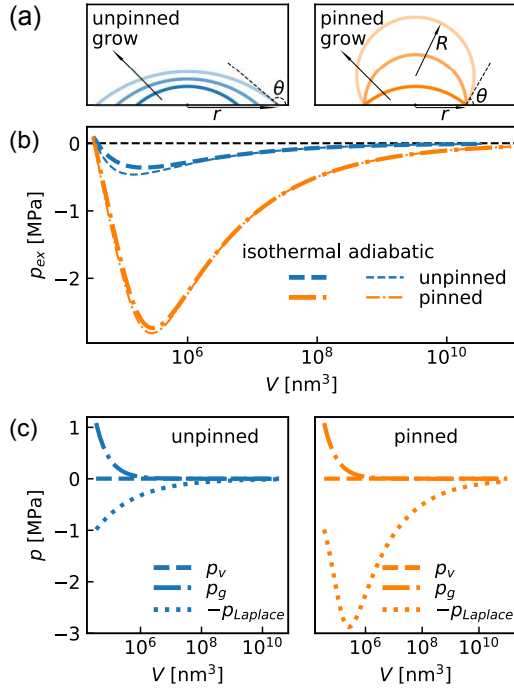


FIG. 1. (a) Schematic illustrating the difference in growth mechanism between unpinned and pinned surface nanobubbles. (b) The change in the excess pressure p_{ex} (see Eq. 3) for growing surface nanobubbles with $r_0 = 50$ nm and $\theta_0 = 160^\circ$ at room temperature and pressure (i.e., $T = T_0 = 298$ K and $p_{atm} = 101.325$ kPa). Results are shown for both isothermal and adiabatic conditions. The horizontal dashed line corresponds to $p_{v,sat} = 3.158$ kPa at $T = 298$ K. (c) The change in the three contributions to p_{ex} , i.e. p_v , p_g and $-p_{Laplace}$, for unpinned and pinned surface nanobubbles under isothermal conditions.

II. THEORY

We first consider an equilibrium surface nanobubble in a liquid with a lateral radius r and a liquid-side contact angle θ [see Fig. 1 (a)]. The bubble is a spherical cap, with a radius of curvature $R = r/\sin \theta$, and volume $V = \pi r^3 g(\theta)/3 \sin^3 \theta$ with $g(\theta) = (2 - \cos \theta)(1 + \cos \theta)^2$. The evolution of an isolated spherical bubble is described by the Rayleigh-Plesset equation [29–31],

$$R\ddot{R} + \frac{3}{2}\dot{R}^2 + 4\nu\frac{\dot{R}}{R} = \frac{p_b(t) - p_l(t) - 2\gamma/R}{\rho_l}. \quad (1)$$

Here, t is the time, ρ_l is the liquid density, γ is the surface tension, ν is the kinematic viscosity of the liquid, $p_l(t)$ is the pressure in the liquid far away from the bubble surface, and $p_b(t)$ is the pressure inside the bubble. The right-hand side in Eq. 1 contains the "forces" driving the bubble to grow or shrink: the collapsing force $F_c = p_l + 2\gamma/R$, which is the sum of the liquid pressure and the Laplace pressure; and the expanding force $F_e = p_b = p_g + p_v$, given by the sum of the gas pressure (p_g) and the vapor pressure (p_v) inside the bubble. In general, the bubble tends to grow if $F_e > F_c$, shrink when $F_e < F_c$, or remain in equilibrium when $F_c = F_e$. A bubble on a solid

surface is expected to undergo a similar evolution to that of a spherical bubble in the bulk [32]. Therefore, assuming that the bubble responds quasi-statically to an external perturbation, we can use the same expansion-collapse criterion to predict its fate under a pressure or temperature change.

The surface nanobubble is in equilibrium at $t = 0$ with $F_c = F_e$, i.e., $p_{l0} + 2\gamma(T_0)/R_0 = p_v(T_0) + p_{g0}$ where T is the temperature and subscript 0 denotes the initial conditions at $t = 0$. If p_{l0} is equal to the atmospheric pressure (p_{atm}), we have

$$p_{g0} = p_{atm} + \frac{2\gamma(T_0) \sin \theta_0}{r_0} - p_v(T_0, r_0, \theta_0). \quad (2)$$

The vapor pressure p_v can be estimated via the Kelvin equation, i.e., $\ln \frac{p_v(T, r, \theta)}{p_{v,sat}(T)} = \frac{-2\gamma(T)V_m(T) \sin \theta}{rRT}$ where $p_{v,sat}$ is the saturated vapor pressure for a flat liquid-vapor interface, \bar{R} the gas constant, and V_m the molar volume of liquid defined as the molar mass (M) divided by its density, i.e., $V_m(T) = M/\rho_l(T)$.

A. No gas diffusion

If the pressure/temperature perturbation takes place too rapidly for significant gas diffusion, there is no appreciable mass transfer of gas to or from the liquid. The evolution of the gas pressure can then be derived in two limiting cases of heat transfer between the liquid and the bubble: 1) isothermal evolution, i.e. the bubble has the same temperature as the liquid, in which case $p_g = p_{g0}V_0T/VT_0$ for an ideal gas; 2) adiabatic evolution, in which $p_g = p_{g0}(V_0/V)^k$ with k the adiabatic index. Considering that unstable growth occurs when $F_e > F_c$ during the whole growth process, this gives us

$$p_l < p_{ex}(r, \theta, T) = p_v(T, r, \theta) - \frac{2\gamma(T) \sin \theta}{r} + p_{g0} \left(\frac{3V_0 \sin^3 \theta}{\pi r^3 g(\theta)} \right)^n \left(\frac{T}{T_0} \right)^m, \quad (3)$$

with $m = n = 1$ for the isothermal evolution and $m = 0$, $n = k$ for the adiabatic evolution. Here $p_{ex}(r, \theta, T)$ denotes the excess pressure against the liquid pressure. We also assume that the vapor pressure and the surface tension only depend on the liquid temperature which is always uniform.

Equation 3 describes the *unstable growth condition* for surface nanobubbles: the excess pressure (p_{ex}) has to be always larger than the liquid pressure (p_l). The change in $p_{ex}(r, \theta, T)$ depends on how the bubble evolves on the substrate. Ideally, we can identify two simplified scenarios [33, 34]: a constant contact angle model (i.e., $\theta \equiv \theta_0$) for unpinned bubbles and a constant lateral radius model (i.e., $r \equiv r_0$) for pinned bubbles [see Fig. 1 (a)]. We note that the unstable growth condition for unpinned bubbles is equivalent to that of bulk spherical bubbles with the same R_0 , and that Eq. 3 leads to the Blake threshold equation for bulk bubbles exposed to a pressure reduction [25, 26] (see Appendix A).

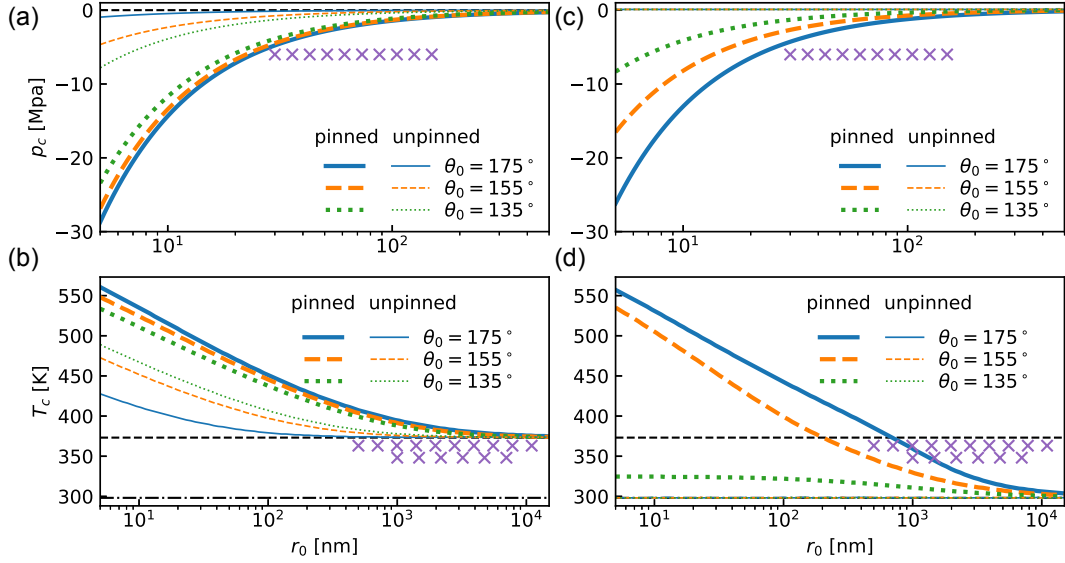


FIG. 2. p_c and T_c in Eq. 3 and Eq. 4 as a function of r_0 when $\theta_0 = 135^\circ$, 155° and 175° for surface nanobubbles in water initially at room temperature and pressure. The purple crosses indicate surface nanobubbles that have been reported to be experimentally stable [24, 27]. (a-b) p_c and T_c with no gas diffusion across the bubble surface and isothermal evolution (i.e., from Eq. 3 with $m = n = 1$). The horizontal dashed lines correspond to $p_{v,sat} = 3.158$ kPa in (a), and the water boiling point 373 K and the room temperature 298 K in (b). (c-d) p_c and T_c with gas equilibration (i.e., from Eq. 4). The horizontal dashed line in (d) corresponds to the boiling point 373 K.

As an example, Figure 1 (b) shows how the $p_{ex}(r, \theta, T)$ given by Eq. 3 changes for surface nanobubbles growing in water at room temperature and pressure (i.e., $T = T_0 = 298$ K and $p_{atm} = 101.325$ kPa) when $r_0 = 50$ nm and $\theta_0 = 160^\circ$. The vapor pressure, the liquid density and the surface tension of water were calculated using the empirical equations in Ref. [35, 36] (see Appendix B), and $k = 1.4$ for the adiabatic evolution. Initially, $p_{ex} = p_l = p_{atm}$, but as the bubble grows p_{ex} decreases to a minimum value, then increases and gradually approaches $p_{v,sat}$. Pinned bubbles, however, have a much lower minimum p_{ex} than unpinned ones, i.e. -0.36 MPa and -0.46 MPa for the former, and -2.74 MPa and -2.81 MPa for the latter. In both cases, a slightly lower minimum p_{ex} is observed for adiabatic vs isothermal conditions.

These results can be understood by considering the three terms that contribute to p_{ex} : the vapor pressure p_v , the gas pressure p_g , and the Laplace term $-p_{Laplace} = -2\gamma \sin \theta / r = -2\gamma / R$. These are plotted independently in Fig. 1 (c) for the isothermal case. For both unpinned and pinned bubbles, p_v remains essentially constant and negligible at room temperature while p_g decreases from p_{g0} as the bubble expands. The change in the Laplace pressure, however, differs qualitatively depending on whether the bubble is pinned or not. For the unpinned bubble, $-p_{Laplace}$ keeps increasing because R always increases during the growth [see the left image in Fig. 1 (a)], which means that p_{ex} only exhibits a minimum because $-p_{Laplace} \propto 1/r$ decays slower than $p_g \propto 1/r^3$ (see Eq. 3). In contrast, for the pinned bubble, $-p_{Laplace}$ decreases while $\theta > 90^\circ$, reaches a minimum at $\theta = 90^\circ$ when $R = r_0$, and then increases for $\theta < 90^\circ$ [see the right image in Fig. 1 (a)]. As a result, the p_{ex} is much larger in magnitude at the critical state.

Due to the influence of p_g , θ at the critical state is smaller than 90° (e.g. $\theta \sim 86^\circ$ at the critical state for the pinned bubble above). In comparison, the adiabatic evolution results in a slightly more negative p_{ex} because $p_g \propto 1/r^{3k}$ decays faster [see Fig. 1 (b)].

To induce unstable growth, one can decrease the liquid pressure until p_l is below a critical pressure p_c equal to the minimum p_{ex} . Our analysis shows that pinned bubbles have much lower p_c than unpinned ones. Alternatively, one can increase the liquid temperature until the minimum p_{ex} is larger than the ambient pressure $p_l = p_{atm}$. Thus, there exists a critical temperature T_c above which unstable growth occurs. Pinned bubbles have higher T_c as p_{ex} is lower. For example, for the surface nanobubbles considered above, $T_c \sim 423$ K if unpinned, while $T_c \sim 473$ K if pinned (see Appendix C). Therefore, pinned surface nanobubbles are much more stable than unpinned ones under either a pressure reduction or a temperature increase.

Figure 2 (a) and (b) give the results for p_c and T_c as a function of r_0 at several values of θ_0 for surface nanobubbles initially at room temperature and pressure and then undergoing isothermal evolution, obtained by numerically solving Eq. 3. For all bubbles, as r_0 increases, p_c increases and gradually approaches $p_{v,sat}(T_0) = 3.158$ kPa, while T_c decreases and approaches the boiling point, i.e. 373 K at 101.325 kPa. However, pinned bubbles have lower p_c and higher T_c compared to unpinned ones with equal r_0 and θ_0 , or to spherical bulk bubbles with the same R_0 (see Appendix A). The differences in p_c and T_c between pinned and unpinned bubbles are large for small r_0 but decrease with increasing r_0 . In addition, as θ_0

increases (i.e., the bubble becomes more flat), p_c increases and T_c decreases for unpinned bubbles, which is in agreement with the observed increase in cavitation on more hydrophobic substrates [32, 37]. In contrast, for pinned bubbles, p_c decreases and T_c increases with growing θ_0 , because flat bubbles contain less gas and therefore have lower p_g and minimum p_{ex} at the critical state. However, as p_g at the critical state contributes little to the minimal p_{ex} , p_c and T_c only depend weakly on θ_0 . Similar behavior is observed under adiabatic conditions, with slightly larger magnitudes for p_c and T_c (see Appendix D).

B. Gas equilibration

The results above are based on the assumption that there is no gas diffusion across the bubble surface during the expansion. This is not valid however, if the pressure or temperature perturbation is slow, such as, when the liquid is experimentally heated by a hot substrate[27]. If there is sufficient time for equilibration to occur, the gas pressure inside the bubble (p_g) can be maintained at a value that depends on the gas concentration in the surrounding liquid (c_g) according to Henry's law, i.e., $p_g = c_g/H$ with H the temperature-dependent Henry's solubility constant and $c_g = p_{g0}H(T_0)$ at the initial equilibrium state. If the liquid can be treated as a gas reservoir with a constant gas concentration and a uniform temperature, the unstable growth condition can be written as

$$p_l < p_{ex}(r, \theta, T) = p_v(T) - \frac{2\gamma(T) \sin \theta}{r} + \frac{p_{g0}H(T_0)}{H(T)}. \quad (4)$$

We therefore calculated p_c and T_c for air surface nanobubbles initially at room temperature and pressure and subsequently evolving with the gas pressure in equilibrium according to Eq. 4. In the calculations, the empirical equation of Henry's solubility constant for the nitrogen in water [38] was used (see Appendix B). The results are given in Fig. 2 (c) and (d), and show how the gas diffusion affects p_c and T_c . First, because unpinned bubbles are unstable under gas equilibration, they always have $p_c = p_{atm}$ and $T_c = T_0$ regardless of the initial size. Second, for pinned bubbles, as r_0 increases, p_c increases and gradually approaches $p_{atm} = 101.325$ kPa. At the same time, under pressure reduction $p_g = p_{g0}H(T_0)/H(T)$ can be constant rather than decreasing rapidly from p_{g0} . This means that p_c will be smaller in magnitude than in the case of no gas diffusion, especially for bubbles with small θ_0 that have high p_{g0} . Third, for pinned bubbles, as r_0 increases, T_c decreases and approaches $T_0 = 298$ K. Furthermore, as H usually decreases with increasing temperature near room temperature, for most bubbles T_c will also be smaller than in the case of no gas diffusion. However, for many species H goes through a minimum (e.g. at ~ 365 K for nitrogen in water) and then increases with increasing temperature [38], so the T_c of very small and flat nanobubbles may be similar to that which one would have without gas diffusion [Fig. 2 (b) and (d)]. Also as p_g contributes more to p_{ex} due to the gas diffusion, the dependence of p_c and T_c on θ_0 becomes more significant.

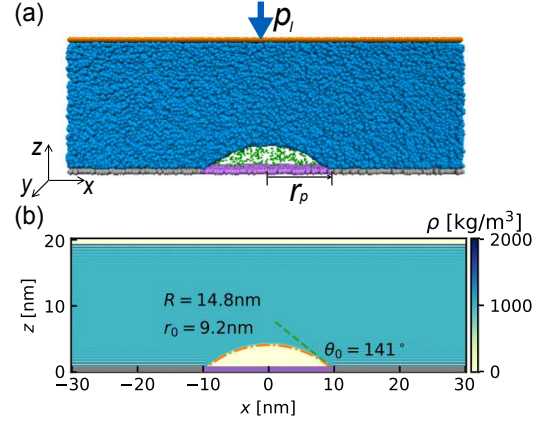


FIG. 3. (a) A typical quasi-2D simulation box with a stable pinned surface nanobubble on a chemically heterogeneous surface at $T = 298$ K and $p_l = 0.1$ Mpa. The box dimensions are: $L_x = 60$ nm, $L_y = 4.25$ nm and $L_z \sim 20$ nm. The blue particles are liquid, green particles are gas, and others are part of solid walls. In the bottom wall, the purple particles form a chemically heterogeneous patch with a width of $2r_p = 20$ nm. (b) Density profile of liquid particles around the pinned bubble in (a). The orange dash-dot line shows the position of the liquid/bubble interface, using a circular fit to the points at which the liquid density is half the bulk value.

Overall, our theoretical analysis predicts that pinned surface nanobubbles can withstand a larger tensile stress (negative pressure) and higher temperatures (i.e., lower p_c and higher T_c) compared to both unpinned bubbles with the same initial contact angle θ_0 and lateral radius r_0 , and free bubbles in the bulk with the same initial radius of curvature R_0 . Bubbles with smaller θ_0 and/or r_0 have larger magnitudes of p_c and T_c , even though, if there is gas diffusion, p_c and T_c can decrease in magnitude making the bubbles less stable. In Sec. IV, we will compare our theoretical analysis with previous experimental results.

III. SIMULATION

To test the validity of our theoretical analysis in the presence of more realistic fluctuations, we used many-body dissipative particle dynamics (MDPD) simulations to predict p_c and T_c for pinned quasi-two-dimensional (quasi-2D) bubbles in a variety of situations.

A. Simulation model and method

Figure 3 shows a typical quasi-2D simulation box with a stable pinned surface nanobubble. The liquid and gas particles are confined between two parallel solid walls. The liquid particles are modeled as MDPD beads [39, 40], which interact with each other via the force $\mathbf{f}_{ij} = A w_c(r_{ij}) \hat{\mathbf{e}}_{ij} + B(\bar{\rho}_i + \bar{\rho}_j) w_d(r_{ij}) \hat{\mathbf{e}}_{ij}$ with i, j particle indices. The first term represents an attractive

TABLE I. Parameters for the Lennard-Jones interaction between different particles.

particles	$\epsilon^{\alpha\beta*}$	$\sigma^{\alpha\beta*}$	$r_{cut}^{\alpha\beta*}$
liquid-gas (lg)	0.4	0.7	$0.7 \cdot (2)^{1/6}$
liquid-top (lt)	0.35	1.0	2.5
liquid-bottom (lb)	0.02 or 0.4	1.0	2.5
gas-gas (gg)	0.4	0.4	1.0
gas-top (gt)	0.4	0.7	$0.7 \cdot (2)^{1/6}$
gas-bottom (gb)	0.4	0.7	$0.7 \cdot (2)^{1/6}$

interaction ($A < 0$) and the second term a many-body repulsive interaction ($B > 0$). $r_{ij} = |\mathbf{r}_{ij}|$ is the distance between the two particles and $\hat{\mathbf{e}}_{ij} = \mathbf{r}_{ij}/r_{ij}$ is the directional unit vector. The weight functions are chosen as $w_c(r_{ij}) = 1 - r_{ij}/r_c$ and $w_d(r_{ij}) = 1 - r_{ij}/r_d$, and become zero at $r_{ij} \geq r_c$ for $w_c(r_{ij})$ and $r_{ij} \geq r_d$ for $w_d(r_{ij})$. The magnitude of the repulsion depends on the local density for each particle which is defined as $\bar{\rho}_i = \sum_{j \neq i} w_\rho(r_{ij})$ with $w_\rho(r_{ij}) = 15(1 - r_{ij}/r_d)^2/2\pi r^3$ if $r_{ij} < r_d$ and $w_\rho(r_{ij}) = 0$ if $r_{ij} \geq r_d$ [39–42].

In our simulations, all units are scaled by the bead mass m , the cutoff radius r_c , and the energy unit e which is equal to the thermal energy $k_B T$ when the simulation temperature $T^* = k_B T/e = 1$ with k_B the Boltzmann constant. Hence, $r_c^* = m^* = e^* = 1$. The superscript asterisk means the quantity is in reduced units. In our simulations, $r_d^* = 0.75$, $A^* = -50$ and $B^* = 25$. To convert to real units, we used the following values: $r_c = 8.5 \text{ \AA}$, $m = 9.0 \times 10^{-26} \text{ kg}$, and $e = 4.1 \times 10^{-21} \text{ J}$, with the characteristic time $\tau = r_c \sqrt{m/e} = 4 \text{ ps}$. Using these parameters, the MDPD liquid at temperature $T^* = 1$ and pressure $p^* = 0.0015$ can approximately reproduce the thermodynamic properties such as the density and the viscosity for bulk water as well as the surface tension for the water-vapor interface at room temperature and pressure [41, 42].

The top and bottom walls are composed of a single layer of particles placed on a simple square lattice with a lattice spacing of $0.5r_c$. The mass $m_g^* = 0.5$ for gas particles and $m_s^* = 1$ for solid particles. The gas and solid particles interact with each other and with liquid beads via the Lennard-Jones (LJ) potential $U^{\alpha\beta}(r) = 4\epsilon^{\alpha\beta}[(\sigma^{\alpha\beta}/r)^{12} - (\sigma^{\alpha\beta}/r)^6]$ truncated and shifted at $r_{cut}^{\alpha\beta}$. Here, r is the distance between two particles, and $\alpha, \beta \in \{\text{liquid, gas, top-wall, bottom-wall}\}$. The LJ parameters are listed in Table I. The bottom wall is chemically heterogeneous in order to pin the bubble, with a hydrophobic patch ($\epsilon^{lb*} = 0.02$ with the equilibrium contact angle $\sim 160^\circ$) at the center and hydrophilic regions ($\epsilon^{lb*} = 0.4$ with the equilibrium contact angle $\sim 53^\circ$) elsewhere. The width of the hydrophobic patch is $2r_p$ [see Fig. 3(a)]. This geometry is convenient to generate “infinite” (i.e. periodically repeated) cylindrical bubbles, whose behaviors are also governed by Eq. 3 and Eq. 4 with some variations to account for the different shapes and the different Laplace pressure contributions. In principle, it is also possible to generate spherical bubbles on circular patch in larger boxes. However, the present approach is more computationally efficient, and thus yields better statistics and more accurate answers.

All simulations were carried out using the parallel molecular dynamics (MD) software package LAMMPS [43, 44]. During the simulations, the top wall was used as a barostat and was free to move as a rigid body in the horizontal and vertical directions. A constant external force along z was imposed on the top wall to maintain the liquid pressure p_l . Each solid particle in the bottom wall was tethered to its initial position via a stiff harmonic potential with spring constant $c^* = 2000$. Periodic boundary conditions were imposed in the x and y directions. The velocity-Verlet algorithm with a time step of 0.003τ (i.e., 12 fs) was used to integrate the equation of motion, and a Nosé–Hoover thermostat with a time constant of 0.3τ was used to maintain the temperature of the liquid and the bottom wall.

We simulated several surface nanobubbles of different sizes (i.e., r_0 and θ_0). The dimensions of the simulation box were adapted to the size of the nanobubble: $L_y = 4.25 \text{ nm}$; $L_x = 6r_p$, with $r_p = 7, 10, \text{ or } 15 \text{ nm}$; and L_z varied with the total number of liquid particles, which was set to 11900, 24200 or 121000, respectively. All bubbles were equilibrated for 1.2 ns at $T_0 = 298 \text{ K}$ and $p_{l0} = 0.1 \text{ MPa}$ starting from an initial cap-shaped configuration. For the stable pinned surface nanobubble, r_0 was inferred from r_p , and θ_0 was controlled by varying the number of gas particles from 80 to 2000. The actual values of r_0 and θ_0 were measured using the density profile of the liquid around the nanobubbles obtained from a 1.2 ns simulation after equilibration [see Fig. 3(b) for an example]. In total, 9 surface nanobubbles with $r_0 = 6\text{--}15 \text{ nm}$ and $\theta = 120^\circ\text{--}150^\circ$ were studied using pressure reduction and temperature increase protocols.

A pressure drop was obtained by instantly reducing the force imposed on the top wall, while the increase in liquid temperature was applied using a linear temperature ramp over 1 ns, to ensure a quasi-static response of the bubble. Note that in our model, the Weeks-Chandler-Andersen (WCA) potential [45] between the liquid and gas particles (see Table I) makes the gas insoluble in the liquid and therefore naturally allows us to mimic the limiting case of no mass transfer to or from the liquid. In order to take gas diffusion into account, we also performed simulations where the number of gas particles was controlled using a grand canonical Monte Carlo algorithm (GCMC) [46] with an ideal gas reservoir of chemical potential $\mu = k_B T_r \ln p_r \Lambda^3 / k_B T_r$, with p_r the reservoir pressure, T_r the reservoir temperature and Λ the thermal wavelength. Considering that in our model the gas is ideal [see Fig. E.1 (a) in Appendix. E], we calculated μ using two different approaches. In the pressure reduction simulations, μ was determined by the initial gas pressure and temperature in the bubble, i.e., $p_r = p_{g0}$ and $T_r = T_0$. In the temperature increase simulations, Henry’s solubility constant cannot be easily determined in our insoluble gas model. We therefore calculated μ using $p_r = p_{g0}$ and set T_r equal to the desired temperature, i.e., $H(T) = H(T_0)$. This is acceptable as we are only concerned about the consequence of gas diffusion. During the simulations, 100 GCMC exchanges were performed every 100 MD steps to achieve gas equilibration between the bubble and the surrounding liquid. All simulations were run for at least 20 ns

to ensure that the bubble was able to reach a new stable state or undergo unstable growth.

B. Simulation results

Figure 4 shows some examples of final states obtained from the pressure reduction and temperature increase simulations with no GCMC exchange for the stable surface nanobubble in Fig. 3 (a). When the pressure is reduced, the bubble expands and is able to reach a stable state at -2.88 Mpa and -5.76 Mpa. At -5.83 Mpa, however, the bubble exhibits unstable growth, and so we conclude that p_c is somewhere between -5.76 and -5.83 Mpa. Similarly, when the temperature is increased, the bubble remains stable until $T = 981$ K, indicating that T_c is somewhere between 978 and 981 K.

The simulation results for p_c and T_c for surface nanobubbles with different values of r_0 and θ_0 are plotted in Fig. 5. In general, these results show the same trends as those obtained from our theoretical analysis. For example, the magnitude of p_c and T_c decreases with increasing r_0 and θ_0 . In the absence of gas diffusion, surface nanobubbles remain stable at temperatures above the boiling point. In contrast, gas diffusion reduces the magnitude of p_c and T_c substantially which, for bubbles with small θ , can cause T_c to drop below the boiling point.

In Fig. 5, we have also plotted the corresponding predictions based on the 2D version of Eq. 3 and Eq. 4 under the condition of $r \equiv r_0$, i.e.,

$$p_l < p_{ex}(r, \theta, T) = p_v(T, r, \theta) - \frac{\gamma(T) \sin \theta}{r} + p_{g0} \left(\frac{A_0}{A} \right)^n \left(\frac{T}{T_0} \right)^m, \quad (5)$$

with the cross-sectional area of the 2D bubble $A = 0.5r^2(\alpha - \sin \alpha)/\sin^2 \theta$ and $\alpha = 2(\pi - \theta)$, and

$$p_l < p_{ex}(r, \theta, T) = p_v(T, r, \theta) - \frac{\gamma(T) \sin \theta}{r} + \frac{p_{g0} H(T_0)}{H(T)}. \quad (6)$$

The thermodynamic properties of the liquid (i.e., the density, the surface tension and the saturated vapor pressure) at different temperatures were obtained by fitting the corresponding data for the MDPD liquid [see Fig. E.1 (b)-(d) in Appendix. E]. In the simulations, the temperature of the bubble was found to always reach the liquid temperature rapidly, indicating that the whole process is almost isothermal. This is the case described by Eq. 5 with $m = n = 1$. This expression, however, overestimates the magnitude of p_c and T_c , especially for the small flat nanobubbles (e.g. with $r_0 \sim 6$ nm and $\theta_0 \sim 150^\circ$). The reason for the discrepancy is that even in the presence of the pinning effect, the contact line exhibits slight expansion during the growth. This can be seen in the simulations (for example in Fig. 4), and makes r increase slightly during the expansion, thereby reducing the magnitude of p_c and T_c . To account for this, we developed an improved theory, in which

the lateral expansion is described by $r = A \cos \theta + B$, where the coefficients A and B are determined by r_0 and θ_0 for various stable pinned surface nanobubbles (see Appendix. F). As can be seen in Fig. 5, the improved theory is much better at predicting p_c and T_c , indicating that the discrepancies from the original theory with $r \equiv r_0$ are mainly due to the lateral expansion. The improved classical theory can predict our simulation results for the stability of pinned surface nanobubbles as small as several nanometers.

IV. DISCUSSION

So far, we have presented our results for the pressure and temperature thresholds (p_c and T_c) beyond which unstable growth occurs for surface nanobubbles when the pressure is reduced or the temperature is increased. In this section, we compare our results with other studies.

Our results for pinned surface nanobubbles under pressure reduction are consistent with those recently reported by Dockar *et al.* [28]. From Eq. 3 and Eq. 5, by computing $p_c = \min(p_{ex})$ at $\partial p_{ex}/\partial \theta = 0$, we can reproduce the equations for the corrected cavitation threshold derived by Dockar *et al.*. In their theoretical calculations they assumed that the maximum gas-side contact angle that a surface nanobubble can sustain is 90° . This assumption was perfectly reasonable, because in their simulations the contact line would unpin at 90° (the equilibrium contact angle on the hydrophilic region), meaning that the gas-side contact angle could never exceed 90° during the expansion. However, if the patch is more hydrophilic, as in our simulations, the pinned bubble will not reach the critical point until the gas-side contact angle is larger than 90° (see Fig. 4). Our analytical theory is able to describe this case as well, without any constraints on θ (see Fig. 1 for example).

Our results also show that the movement of the contact line can significantly affect p_c and T_c . For example, the "stick-jump" behavior in Dockar *et al.*'s simulations decreases the magnitudes of p_c and T_c compared to that expected for ideally pinned bubbles. Another example is the slight lateral expansion of the contact line observed in our simulations during growth, which also decreases the magnitudes of p_c and T_c (see Fig. 5). The actual behavior of the contact line in an experimental system will strongly depend on the physical and chemical properties of the substrate and could be very complex [34, 47]. The theoretical results in the case of ideal pinning (i.e., $r \equiv r_0$) describe maximally stable surface nanobubbles, i.e., they predict extrema for p_c and T_c . In order to obtain more precise predictions from classical theory, the effect of the contact line dynamics needs to be taken into account, such as in our modified theory that includes the effect of the lateral expansion.

Our theoretical calculations (both original and modified) predict that surface nanobubbles with $r_0 > 25$ nm should undergo unstable growth at -6 Mpa, but an earlier experiment [24] reported that surface nanobubbles with $r_0 = 30$ – 150 nm remain stable up to -6 Mpa [see Fig. 2 (a) and (c)]. This disagreement could be due to the specific protocol followed

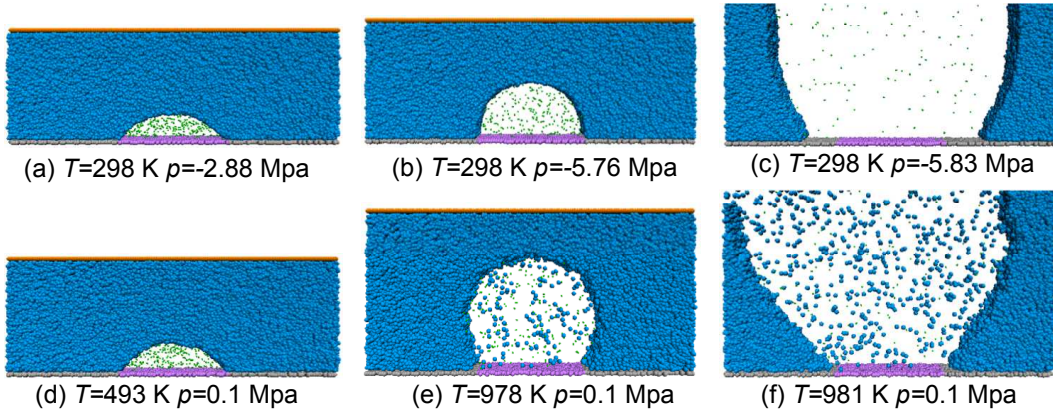


FIG. 4. Snapshots of the final states obtained from the pressure reduction and temperature increase simulations, at the indicated pressures and temperatures, starting from the stable surface nanobubble in Fig. 3 (a). The bubbles in (c) and (f) are unstable. Note that no gas diffusion across the bubble interface was allowed in these simulations.

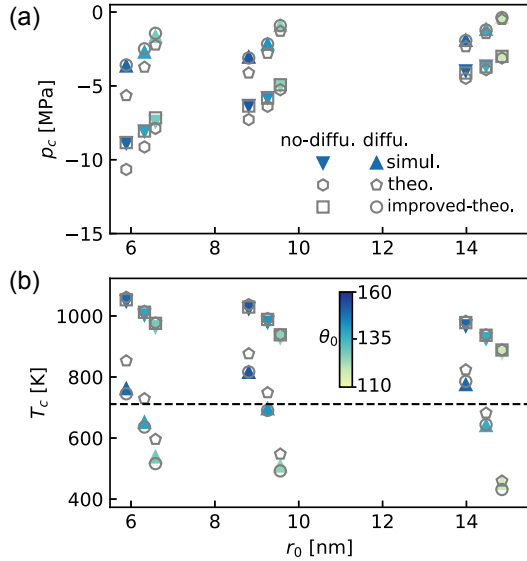


FIG. 5. Critical pressures (p_c) and temperatures (T_c) for pinned surface nanobubbles with different initial values of r_0 and θ_0 . Results from the MDPD simulations and theoretical analysis (Eq. 5 with $m = n = 1$ and Eq. 6) are compared. In addition, results are shown for an improved theory, in which lateral expansion of the contact line is taken into account. The horizontal dashed line in (b) corresponds to the boiling point of the MDPD liquid, which is 711 K at 0.1 MPa [see Fig. E.1 (b) in Appendix. E].

in the experiment where the pressure perturbation was generated by a shock wave with both compression and expansion phases. As pointed out by the authors, the original nanobubbles may be removed during the initial rapid compression phase and different bubbles could form under the following negative pressure [24]. Dockar *et al.* also noticed this discrepancy and hypothesized a possible mechanism by which the bubbles detaching from the surface during unstable growth could form

more stable bulk nanobubbles with a reduced radius of curvature [28]. It is also possible that contamination [48], surface charges [49] or collective effects [32] could be responsible for the abnormal stability reported in these experiments.

Finally, the upper critical temperature for stability of surface nanobubbles has also been investigated experimentally [27]. We have plotted this data as crosses in Fig. 2 (b) and (d). If there is no gas diffusion, all pinned surface nanobubbles are predicted to be stable below the boiling temperature, and the classical theory is able to explain the experimental results. However, gas diffusion should be non-negligible in these experiments because the liquid was slowly heated by a hot substrate. If the gas diffusion was sufficiently fast to allow for equilibration between the bubble and the water, as we considered above, then only small flat nanobubbles should be stable. A possible reason for this discrepancy is that diffusion of gas also occurs from the water into the surrounding environment, thus reducing the gas concentration in the liquid and moving T_c back towards the boiling point.

V. SUMMARY

In this work, we investigated the stability of pinned surface nanobubbles exposed to a reduction in pressure or an increase in temperature. The pressure and temperature thresholds (p_c and T_c) at which unstable growth occurs for surface nanobubbles in water were first determined using the expansion-collapse criterion from the classical Rayleigh-Plesset theory (Eq. 3 and Eq. 4). Due to contact line pinning, surface nanobubbles grow with a nearly constant lateral radius, and consequently a reduced radius of curvature, resulting in a lower p_c and higher T_c compared to unpinned bubbles with the same initial contact angle and lateral radius (θ_0 and r_0) or bulk bubbles with the same initial radius of curvature (R_0). p_c and T_c are dependent on both θ_0 and r_0 , and decreasing θ_0 and/or

r_0 increases the magnitude of p_c and T_c , making the bubbles more stable. On the other hand, gas diffusion between the bubble and the liquid can decrease the magnitude of p_c and T_c . The values of p_c and T_c obtained from MDPD simulations of quasi-2D surface nanobubbles are consistent with our theoretical predictions, provided that we account for the lateral expansion of the contact line that occurs in our simulations during bubble growth. This validates our classical thermodynamic description for pinned surface nanobubbles as small as several nanometers. Even though our predictions for p_c and T_c are inconsistent with some experimental results, we would like to point out that these discrepancies could be attributed to the high uncertainties in bubble dynamics and gas diffusion inherent in current experimental techniques. We hope that our

work will inspire further theoretical and experimental studies that will ultimately yield a more comprehensive understanding of surface nanobubble stability.

ACKNOWLEDGMENTS

This work was supported by the Australian Research Council under Grant CE170100026. Computational resources were provided by the University of Sydney HPC service, and the Pawsey Supercomputing Centre with funding from the Australian Government and the Government of Western Australia.

-
- [1] J. L. Parker, P. M. Claesson, and P. Attard, *J. Chem. Phys.* **98**, 8468 (1994).
 - [2] S.-T. Lou, Z.-Q. Ouyang, Y. Zhang, X.-J. Li, J. Hu, M.-Q. Li, and F.-J. Yang, *J. Vac. Sci. Technol. B Microelectron. Nanom. Struct.* **18**, 2573 (2000).
 - [3] N. Ishida, T. Inoue, M. Miyahara, and K. Higashitani, *Langmuir* **16**, 6377 (2000).
 - [4] P. S. Epstein and M. S. Plesset, *J. Chem. Phys.* **18**, 1505 (1950).
 - [5] D. Lohse and X. Zhang, *Rev. Mod. Phys.* **87**, 981 (2015).
 - [6] M. Alheshibri, J. Qian, M. Jehannin, and V. S. Craig, *Langmuir* **32**, 11086 (2016).
 - [7] X. H. Zhang, N. Maeda, and V. S. Craig, *Langmuir* **22**, 5025 (2006).
 - [8] M. Switkes and J. W. Ruberti, *Appl. Phys. Lett.* **84**, 4759 (2004).
 - [9] R. Steitz, T. Gutberlet, T. Hauss, B. Klösgen, R. Krastev, S. Schemmel, A. C. Simonsen, and G. H. Findenegg, *Langmuir* **19**, 2409 (2003).
 - [10] S. Karpitschka, E. Dietrich, J. R. Seddon, H. J. Zandvliet, D. Lohse, and H. Riegler, *Phys. Rev. Lett.* **109**, 66102 (2012).
 - [11] C. U. Chan and C. D. Ohl, *Phys. Rev. Lett.* **109**, 174501 (2012).
 - [12] X. Zhang, D. Y. Chan, D. Wang, and N. Maeda, *Langmuir* **29**, 1017 (2013).
 - [13] J. H. Weijs and D. Lohse, *Phys. Rev. Lett.* **110**, 054501 (2013).
 - [14] Y. Liu and X. Zhang, *J. Chem. Phys.* **138**, 014706 (2013).
 - [15] D. Lohse and X. Zhang, *Phys. Rev. E* **91**, 031003 (2015).
 - [16] C. U. Chan, L. Chen, M. Arora, and C. D. Ohl, *Phys. Rev. Lett.* **114**, 114505 (2015).
 - [17] Z. Guo, Y. Liu, Q. Xiao, H. Schönherr, and X. Zhang, *Langmuir* **32**, 751 (2016).
 - [18] B. Dollet and D. Lohse, *Langmuir* **32**, 11335 (2016).
 - [19] S. Maheshwari, M. Van Der Hoef, X. Zhang, and D. Lohse, *Langmuir* **32**, 11116 (2016).
 - [20] Q. Xiao, Y. Liu, Z. Guo, Z. Liu, and X. Zhang, *Appl. Phys. Lett.* **111**, 131601 (2017).
 - [21] B. H. Tan, H. An, and C. D. Ohl, *Phys. Rev. Lett.* **118**, 054501 (2017).
 - [22] B. H. Tan, H. An, and C.-D. Ohl, *Phys. Rev. Lett.* **120**, 164502 (2018).
 - [23] S. Maheshwari, M. Van Der Hoef, J. Rodríguez Rodríguez, and D. Lohse, *ACS Nano* **12**, 2603 (2018).
 - [24] B. M. Borkent, S. M. Dammer, H. Schönherr, G. J. Vancso, and D. Lohse, *Phys. Rev. Lett.* **98**, 204502 (2007).
 - [25] F. Blake, *Onset of Cavitation in Liquids*, Technical memorandum (Harvard University, 1949).
 - [26] C. E. Brennen, *Cavitation and bubble dynamics* (Oxford University, New York, 1995).
 - [27] X. Zhang, H. Lhuissier, C. Sun, and D. Lohse, *Phys. Rev. Lett.* **112**, 144503 (2014).
 - [28] D. Dockar, M. K. Borg, and J. M. Reese, *Langmuir* **35**, 9325 (2019).
 - [29] L. Rayleigh, *London, Edinburgh, Dublin Philos. Mag. J. Sci.* **34**, 94 (1917).
 - [30] M. S. Plesset, *J. Appl. Mech.* **16**, 277 (1949).
 - [31] M. S. Plesset and A. Prosperetti, *Annu. Rev. Fluid Mech.* **9**, 145 (1977).
 - [32] N. Bremond, M. Arora, S. M. Dammer, and D. Lohse, *Phys. Fluids* **18**, 121505 (2006).
 - [33] Y. Liu and X. Zhang, *Phys. Rev. E* **88**, 012404 (2013).
 - [34] J. H. Snoeijer and B. Andreotti, *Annu. Rev. Fluid Mech.* **45**, 269 (2013).
 - [35] N. B. Vargaftik, B. N. Volkov, and L. D. Voljak, *J. Phys. Chem. Ref. Data* **12**, 817 (1983).
 - [36] W. Wagner and A. Pruss, *J. Phys. Chem. Ref. Data* **22**, 783 (1993).
 - [37] V. Belova, D. A. Gorin, D. G. Shchukin, and H. Möhwald, *ACS Appl. Mater. Interfaces* **3**, 417 (2011).
 - [38] A. H. Harvey, *AIChE J.* **42**, 1491 (1996).
 - [39] I. Pagonabarraga and D. Frenkel, *J. Chem. Phys.* **115**, 5015 (2001).
 - [40] M. Arienti, W. Pan, X. Li, and G. Karniadakis, *J. Chem. Phys.* **134**, 204114 (2011).
 - [41] A. Ghoufi and P. Malfreyt, *Phys. Rev. E* **83**, 051601 (2011).
 - [42] A. Ghoufi, J. Emile, and P. Malfreyt, *Eur. Phys. J. E* **36**, 10 (2013).
 - [43] S. Plimpton, *J. Comput. Phys.* **117**, 1 (1995).
 - [44] Z. Li, G.-H. Hu, Z.-L. Wang, Y.-B. Ma, and Z.-W. Zhou, *Phys. Fluids* **25**, 072103 (2013).
 - [45] J. D. Weeks, D. Chandler, and H. C. Andersen, *J. Chem. Phys.* **54**, 5237 (1971).
 - [46] D. Frenkel and B. Smit, *Understanding molecular simulation: from algorithms to applications, 2nd Edition* (Elsevier, 2010) pp. 205–212.
 - [47] Y. Liu, J. Wang, X. Zhang, and W. Wang, *J. Chem. Phys.* **140**, 054705 (2014).
 - [48] W. A. Ducker, *Langmuir* **25**, 8907 (2009).
 - [49] S. O. Yurchenko, A. V. Shkirin, B. W. Ninham, A. A. Sychev, V. A. Babenko, N. V. Penkov, N. P. Kryuchkov, and N. F. Bunkin, *Langmuir* **32**, 11245 (2016).

Appendix A: Unstable growth condition for free spherical bubbles

Similarly to what shown in the main text, it is easy to derive the unstable growth condition for free spherical bubbles with initial radius R_0 and initial gas pressure $p_{g0} = p_{atm} + 2\gamma(T_0)/R_0 - p_v(T_0)$, i.e.

$$p_l < p_{ex}(R, T) = p_v(T) - \frac{2\gamma(T)}{R} + p_{g0} \left(\frac{3V_0^B}{4\pi R^3} \right)^n \left(\frac{T}{T_0} \right)^m. \quad (A1)$$

with V_0^B the initial volume of the bulk bubble. The minimum liquid pressure that satisfies Eq. A1 is often called the Blake threshold for bubbles under pressure reduction (i.e., $T = T_0$) [25, 26] and can be obtained at $\partial p_{ex}/\partial R = 0$, i.e.,

$$p_B = \min(p_{ex}) = p_v - 2\gamma \left(1 - \frac{1}{3n} \right) \left(\frac{\gamma}{3nR_0^{3n}p_{g0}} \right)^{1/(3n-1)}. \quad (A2)$$

The unstable growth condition for surface nanobubbles can also be written with respect to the radius of curvature R , and the initial bubble volume $V_0 = V_0^B g(\theta_0)/4$ with V_0^B the volume of a bulk spherical bubble of the same R_0 . Thus, Eq. 3 can be rewritten as

$$p_l < p_{ex}(R, \theta, T) = p_v(T) - \frac{2\gamma(T)}{R} + p_{g0} \left(\frac{3V_0^B g(\theta_0)}{4\pi R^3 g(\theta)} \right)^n \left(\frac{T}{T_0} \right)^m. \quad (A3)$$

If the surface nanobubble evolves with a constant contact angle (i.e., $\theta \equiv \theta_0$), Eq. A3 will become exactly the same as Eq. A1 because $g(\theta) \equiv g(\theta_0)$ and will lead to the same Blake threshold as Eq. A2. Therefore, an unpinned surface nanobubble should have the same p_c and T_c as that of a free bubble with the same R_0 [32].

Appendix B: Thermodynamic properties of water and air

The thermodynamic properties of water and Henry's solubility constant for nitrogen in water were calculated using empirical equations [35, 36, 38]. The critical temperature $T_c = 647.15$ K, the critical saturated vapor pressure $p_{v,c} = 22.064 \times 10^6$ Pa and the critical liquid density $\rho_c = 322$ kg/m³.

- The saturated vapor pressure ($p_{v,sat}$ [Pa]) is given by

$$\ln \left(\frac{p_{v,sat}}{p_{v,c}} \right) = \frac{T_c}{T} [a_1\tau + a_2\tau^{1.5} + a_3\tau^3 + a_4\tau^{3.5} + a_5\tau^4 + a_6\tau^{7.5}] \quad (B1)$$

with $a_1 = -7.85951783$, $a_2 = 1.84408259$, $a_3 = -11.7866497$, $a_4 = 22.6807411$, $a_5 = -15.9618719$, and $a_6 = 1.80122502$.

- The liquid density (ρ_l [kg/m³]) is given by

$$\frac{\rho_l}{\rho_c} = 1 + b_1\tau^{1/3} + b_2\tau^{2/3} + b_3\tau^{5/3} + b_4\tau^{16/3} + b_5\tau^{43/3} + b_6\tau^{110/3} \quad (B2)$$

with $b_1 = 1.99274064$, $b_2 = 1.09965342$, $b_3 = -0.510839303$, $b_4 = -1.75493479$, $b_5 = -45.5170352$, and $b_6 = -6.74694450 \times 10^5$.

- The surface tension (γ [N/m]) is given by

$$\gamma = B \left[\frac{T_c - T}{T_c} \right]^\mu \left[1 + b \left(\frac{T_c - T}{T_c} \right) \right], \quad (B3)$$

with $B = 0.2358$, $\mu = 1.256$, $b = -0.625$.

- Henry's solubility constant (H [mol/m³/MPa]) for nitrogen in water is given by

$$\ln \frac{M}{H\rho_l} = \frac{A}{T/T_c} + B \frac{(1 - T/T_c)^{0.355}}{T/T_c} + C \exp(1 - T/T_c)(T/T_c)^{-0.41} + \ln p_{v,sat} \quad (B4)$$

with $B = -11.6184$, $B = 4.9266$, $C = 13.3445$.

Appendix C: Change of excess pressure at different temperatures

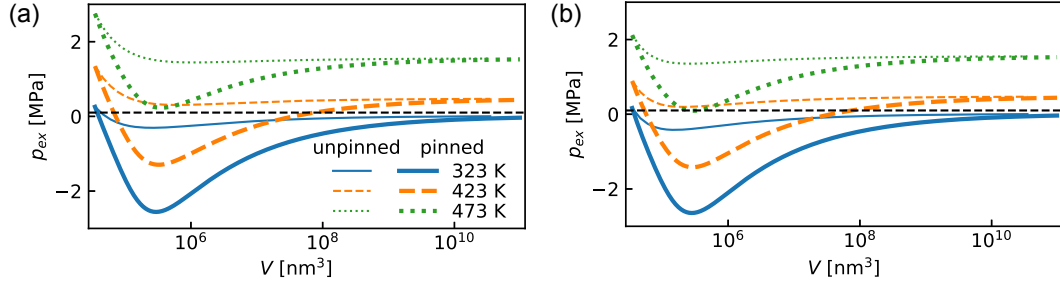


FIG. C.1. Change in excess pressure p_{ex} (see Eq. 3) for growing surface nanobubbles with $r_0 = 50$ nm and $\theta_0 = 160^\circ$, initially at room temperature and pressure, and then undergoing isothermal (a) or adiabatic (b) evolution at three different temperatures. The horizontal dashed line corresponds to $p_l = p_{atm} = 101.325$ kPa.

Appendix D: Pressure and temperature thresholds for bubbles under adiabatic condition

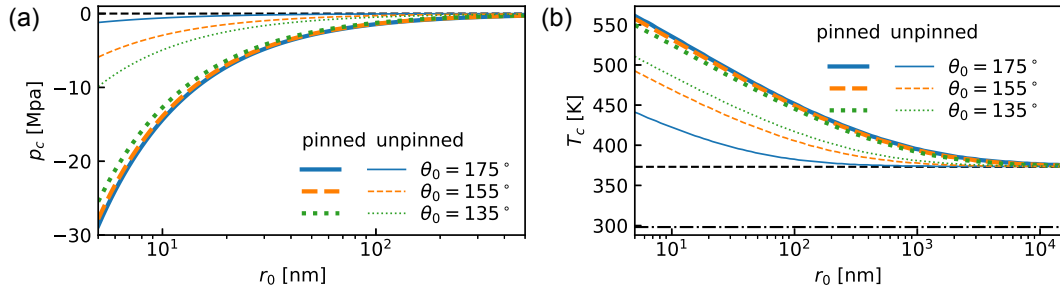


FIG. D.1. p_c (a) and T_c (b) as a function of r_0 (see Eq. 3) at $\theta_0 = 135^\circ$, 155° and 175° for surface nanobubbles initially at room temperature and pressure, and then undergoing adiabatic evolution. The horizontal dashed lines correspond to $p_{v,sat} = 3.158$ kPa in (a), and the boiling point 373 K and room temperature 298 K in (b).

Appendix E: Thermodynamic properties of gas and liquid in the MDPD simulation model

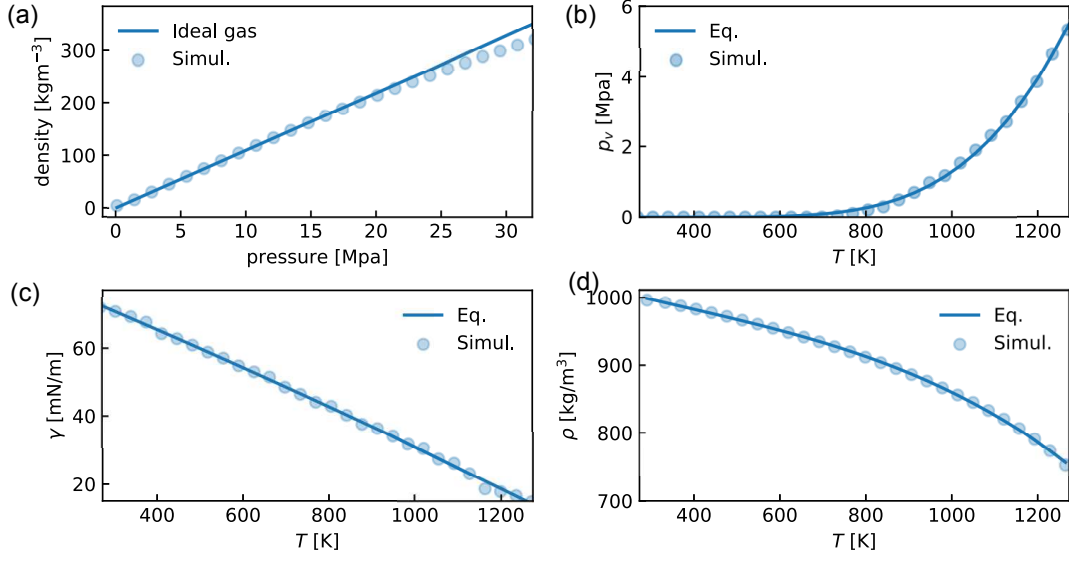


FIG. E.1. (a) Gas density at different pressures and at 298 K. The solid line is the equation-of-state for the ideal gas. The data were obtained from a simulation with 1000 gas particles in a cubic box. (b-d) Thermodynamic properties of the MDPD liquid. (b) Saturated vapor pressure at different temperatures. The boiling point at 0.1 Mpa is 711 K. The fitting equation is $\log_{10} p_v = A - (B/(C + T))$ with $A = 9.41847$, $B = 3833.13$ and $C = 157.658$. (c) Surface tension for the liquid-vapor interface at different temperatures. At 298 K, the surface tension is 71 mN/m, which is very close to the value of water at the same temperature. The fitting equation is $\gamma = aT^2 + bT + c$ with $a = -3.97652 \times 10^{-9}$, $b = -5.22706 \times 10^{-5}$ and $c = 8.70742 \times 10^{-2}$. (d) Density at different temperatures at 0.1 Mpa. At 298 K, the density is 997 kg/m³. The fitting equation is $\rho = aT^3 + bT^2 + cT + d$ with $a = -1.42055 \times 10^{-7}$, $b = 1.63578 \times 10^{-4}$, $c = -2.11321 \times 10^{-1}$ and $d = 1.04993 \times 10^9$. The data for saturated vapor pressure and surface tension were obtained from a simulation with one liquid slab consisting of 1000 MDPD particles in a rectangular simulation box with edges $L_x = L_y = 8.5$ nm and $L_z = 17$ nm. The data for the density were obtained from a simulation with 1000 MDPD particles in a cubic box.

Appendix F: Relation between lateral radii and contact angles for pinned surface nanobubbles

In our simulations, we found that the lateral radius (r) is approximately a linear function of the cosine of the liquid-side contact angle (θ) for stable pinned surface nanobubbles on substrates with a hydrophobic patch of width $2r_p$ (see Fig. F.1). We assume that when the surface nanobubble expands quasi-statically, the lateral radius obeys the same linear relationship between r and $\cos \theta$, i.e., $r = A \cos \theta + B$. The values of A and B at several different values of r_p are given in Table. F.1.

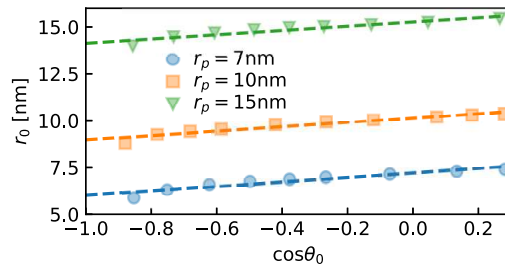


FIG. F.1. Dependence of r_0 on $\cos \theta_0$ for stable surface nanobubbles when $r_p = 7, 10$ and 15 nm. The dashed lines show the linear fits listed in Table. F.1

TABLE F.1. Coefficients for the linear fit $r = A \cos \theta + B$ at the indicated values of r_p .

r_p [nm]	A [nm]	B [nm]
7	1.480	7.376
10	1.488	10.345
15	1.437	15.433